Materials Characterization 191 (2022) 112166

Contents lists available at ScienceDirect

Materials Characterization

journal homepage: www.elsevier.com/locate/matchar

The dependency of work hardening on dislocation statistics in cold rolled 1050 aluminum alloy

Purnima Chakravarty [a,b,*], Gyula Pál [a,b], Jurij J. Sidor [a,*]

[a] Savaria Institute of Technology, Faculty of Informatics, Eötvös Loránd University (ELTE), Károlyi Gáspár tér 4, 9700 Szombathely, Hungary
[b] Doctoral School of Physics, Faculty of Natural Sciences, Eötvös Loránd University (ELTE), P.O. Box 32, 1518 Budapest, Hungary

ARTICLE INFO

Keywords:
Work hardening
Dislocation density
Stored energy
GND
SSD

ABSTRACT

In this contribution, the phenomenon of work hardening is studied as a function of the nature of dislocation evolution with change in the level of deformation for commercially available 1050 Al alloy. To investigate the nature of dislocations in the cold-rolled aluminum alloy, total dislocation density was calculated using the indentation technique as well as by implementing two numerical approaches. For estimation of a statistically representative value of geometrically necessary dislocations (GND), electron backscattering diffraction measurements were performed over a large area (~ 0.5 mm^2). The GND density of deformed samples was quantified by the implementation of a modified kernel average misorientation technique as well as by using Nye's dislocation density tensor for corresponding lattice curvature. The values of statistically stored dislocations (SSD) are obtained based on the assessment of the total dislocation density and GND values after different straining levels. The study provides both qualitative and quantitative illustrations of the mechanism of dislocation multiplication as thickness reduction increases, thereby, increasing the hardness of the samples. The results obtained reveal that the hardening of rolled materials is majorly governed by the SSD density at lower deformation. However, as the deformation level approaches the value of ~0.4, the density of GNDs rises and its contribution becomes significantly accountable for the strain hardening of the material. On the other hand, it has been observed that at lower straining levels the generated GNDs are trapped at grain boundaries and have a high contribution towards forest dislocations but with an increase of strain, the GNDs have a tendency to contribute nearly equally to mobile and forest dislocations. The estimated stored energies for samples subjected to rolling reduction ranging between 5.3 and 76% tend to change between the 5.6 kJ/m^3 and 343.3 kJ/m^3.

1. Introduction

The phenomenon of plastic deformation in metals is dominated by the complex mechanism of dislocation glide over the slip planes. On the microscopic level, the generation, motion, subsequent trapping, and deposition of dislocations play an important role in the work hardening of the metal alloys [1,2]. This results in a high scientific demand for escalation of dislocation density in material to study the state of deformation [3]. Hence, to have a better understanding of the phenomenon of work hardening it is important to analyze the evolution of dislocation structure for the material under consideration [1–3].

There are various direct and indirect techniques to assess the total dislocation density (ρ), such as transmission electron microscopy (TEM) [4], X-ray line profile analysis (XPLA) [3], indentation technique [5], and Electron Backscattering diffraction (EBSD) [6]. Several modelling approaches allowing estimation of ρ, for example, Kubin- Estrin (K-E) [7] and simplified K-E [8,9] models claim to approximate the dislocation density efficiently. It has been shown [5] that the indentation technique is an effective approach allowing the evaluation of dislocation density over a large area. The estimated dislocation density values are comparable to ones obtained by the XPLA under the range of experimental error. The microindentation is found to be a quantitively more effective tool to estimate the amount of dislocations as compared to other techniques, as well as proficient in terms of time and expenses. In this methodology the dislocation density is estimated using the following relationship [5]:

* Corresponding authors at: Savaria Institute of Technology, Faculty of Informatics, Eötvös Loránd University (ELTE), Károlyi Gáspár tér 4, 9700 Szombathely, Hungary.
E-mail addresses: pc@inf.elte.hu (P. Chakravarty), pg@inf.elte.hu (G. Pál), js@inf.elte.hu (J.J. Sidor).

https://doi.org/10.1016/j.matchar.2022.112166
Received 20 June 2022; Received in revised form 22 July 2022; Accepted 24 July 2022
Available online 27 July 2022

$$\rho = \frac{1}{\alpha^3}\left(\frac{H_v}{3.06MGb}\right)^2 \quad (1)$$

where, H_V is Vickers hardness, M is the Taylor factor, G is the shear modulus and α is the geometric constant [5,10,11], and b is a Burgers vector.

In Eq. (1), the value of ρ is estimated as a function of the hardness response of the material, while in numerical models of Kubin- Estrin (K-E) [7] or modified K-E [8,9], the dislocation density is calculated as a direct function of applied strain (e). The K-E model estimates dislocation density as the sum of mobile (ρ_m) and forest (ρ_f, immobile) counterparts i.e. $\rho = \rho_m + \rho_f$ [7]. The frame of the K-E approach is expressed as follows:

$$\frac{d\rho_m}{de} = C_1 - C_2\rho_m - C_3\rho_f^{\frac{1}{2}} \quad (2a)$$

$$\frac{d\rho_f}{de} = C_2\rho_m + C_3\rho_f^{\frac{1}{2}} - C_4\rho_f \quad (2b)$$

Where, C_i are material constants.

The density of both dislocation types is responsible for the characteristic features of plastic behavior and has a strong relationship with the hardness impartment in the material [12]. In Eqs. (2a) and (2b), the parameters C_i take accountability for various fundamental microscopic processes that occur in the course of plastic deformation. For example, coefficients C_1 and C_2 represent the effect of the multiplication of mobile dislocations and their significant trapping, whereas the response of immobilization via interaction with the forest dislocations is taken into account by the C_3 parameter. The phenomenon of dynamic recovery is governed by the C_4 model parameter [7,12]. The K-E model is further simplified by Csanádi et al. [8,9], where the total dislocation density is calculated as the sum of its mobile and forest counterparts. It was found that the model parameters C_1 and C_2 are nearly identical for various metals, subjected to different thermomechanical processing, and hence, the simplified K-E model was formulated as following [8,9]:

$$\rho(e) = \frac{2C_1}{C_4} - \left(\frac{2C_1}{C_4} - \rho_0\right)\left(1 + \frac{C_4 e}{2}\right)exp(-C_4 e) \quad (3)$$

The generation of dislocations follows a convoluted path by the formation of Geometrically Necessary Dislocations and Statistically Stored Dislocations. In case of polycrystalline or multiphase alloys, deformation gradient forms due to inhomogeneous plastic deformation throughout the matter, which is stored in the system in form of GNDs [13]. In other words, Geometrically Necessary Boundaries (GNBs) evolve, because of different magnitudes of plastic slip of corresponding slip systems among neighboring regions of the grains, which induce the process of grain subdivision into cell blocks. To accommodate lattice misorientation near GNBs, geometrically necessary dislocations emerge thereby aligning themselves at the boundaries [13,14]. On the other hand, the evolution of SSDs is not ruled by any geometric factor; rather they pile up due to statistical trapping of dislocations during the inelastic slip. This is the major reason behind the random distribution of SSDs in a heterogeneous mosaic pattern at the microscale, consisting of other substructures [13–15]. It can be summarized here that GNDs are steaming from the heterogeneity in the process of deformation, while SSDs are associated with homogeneous deformation. However, as it was highlighted elsewhere [16,17] there is no qualitative difference between the SSDs and GNDs, the variety can be described only in terms of formation mechanism and distributional parameters. It has also been reported that it might be challenging to obtain a scalable analysis of SSDs, which is described in terms of starting from the quantity of data among a large number of grains to setting up other parameters like time of scan and isolation of GNDs and SSDs in Transmission Electron Microscopy (TEM) [18]. However, it is well known that the quantity of GNDs can be credibly accounted by using the EBSD technique, and subtracting them from the total dislocation density makes possible the quantification of SSDs [13,19].

It is possible to calculate GNDs from the EBSD data either by estimating the lattice curvature or *curl* of the orientation field associated with Nye's tensor component fields employing orientation maps or by computing Kernel Average Misorientation (KAM) [5,20]. In the case of EBSD scans, choosing a compatible Burgers circuit plays a key role as the Burgers circuit is related to the step size under consideration. A larger size of Burgers circuit can arise a situation where most of the dislocations within the circuit will interact with dislocations of opposite signs, forming dislocation dipoles or multipoles which capture no net geometric consequences [13,17,18]. On the other hand, if the Burgers circuit or step size is small enough it can separate these poles and ensure a high accuracy by capturing a significant fraction of GNDs from the total dislocation density [17,18,21]. It has been reported that the appropriate step size for GND scan should be comparable to the length scale of the dislocation cell structure or even smaller. In this way, the better countability of most of the dislocation networks can be captured [21,22]. Special care should be taken while choosing the appropriate neighbor rank (step size/kernel radius) on the scan as the distortion gradient is a direct function of the selected rank of the neighbor. In the case of calculating GNDs from the misorientation angle calculated for neighboring rank, the failure in choosing the appropriate kernel radius can lead to overestimation of GND density by taking noise under consideration [16,22,23]. In the current work, the GND density is calculated using both Nye's tensor components corresponding to the orientation field and KAM angle. The comparative analysis of both techniques in calculating GND will guide towards choosing efficient parameters. While calculating GNDs from KAM, to avoid-above mentioned shortcomings such as the effect of noise and high dependency on step size, the data has been processed as per Kamaya's approach [24,25].

The misorientation angle obtained from KAM represents the average misorientation angle of a point of reference to its neighbors in the EBSD map, which is the quantification of the local misorientation level, i.e., GND. [24–26]. The simplified model of calculating GND density from misorientation angle was proposed by Read and Shockley [26], which is given as follows:

$$\rho_{GND} = \frac{k < \theta >}{bs} \quad (4)$$

In Eq. (4), k is a constant that depends on the type of dislocation and s is the distance between the two points for which the kernel average misorientation angle (θ) has been calculated, i.e., step size [24–26].

In the present study, the quantitative understanding of the total dislocation density and the respective constitutes of ρ is employed to explain the evolution of work hardening in the cold-rolled 1050 Al alloy. Both, total dislocation density and the GNDs have been derived using microindentation and EBSD techniques. The strain hardening of cold deformed sheets were investigated because of (i) industrial importance and (ii) due to the limitations of tensile test, which is not capable of providing information on hardening phenomena at high strains (1 or even higher) due to restricted maximum elongation of samples (typically, the total elongation reached in tension is ~50%).

2. Materials and method

The investigated 1050 Al alloy is a commercially available material with Al-0.3 wt% Fe, providing minimum solute content and making it one of the most fundamental Al systems. The initial material (Sample A) was subjected to full recrystallization by annealing at 550 °C and followed by symmetric cold rolling with thickness reductions of 5.3% (sample B), 15.8% (sample C), 21.1% (sample D), 28.9% (sample E), 40% (Sample F), 46.8% (sample G), 60% (sample H) and 76% (sample I). The rolling experiments were performed in a single pass with an absence of lubricant using a laboratory rolling machine with a roll diameter of 150 mm.

To study the evolution of dislocation density from respective hardness values of the annealed and deformed samples, indentation measurements were performed using the Zwick/Roell® ZHVμ-type Vickers microhardness tester. Prior to the test, the samples were subjected to the standard sample preparation procedure, which includes mechanical grinding and mechanical polishing. The mechanical polishing of the samples was performed using Struers®-type DiaDuo suspensions of 3 μm and 1 μm diamond particles. After mechanical polishing, the investigated samples were soap cleaned under running water and dried. The Vickers hardness test was conducted for loads under the range of 100gf to 500gf by initiating diamond-shaped indents on the Normal Direction (ND) plane through the sub-surface of the samples. The applied load range was chosen to avoid the indentation size effect (ISE) [27].

For the assessment of GND density as well as texture measurements and other microstructural investigations, samples A-I were exposed to EBSD scans across the thickness. During the EBSD experiments, the electron beam scanned the investigated area and recorded a quantitative measure of the quality of Kikuchi patterns obtained from each point [28]. The EBSD maps were captured using the Hikari-type® detector attached to a high-resolution scanning electron microscope with a FEG filament. The mechanically grinded and polished samples were electropolished prior to EBSD scans. The electrolytic polishing of the samples was performed using cooled (0–5 °C) Struers® A2 electrolyte at a voltage ranging from 20 V to 30 V for 45–60 s. The EBSD scanning was performed in two slots for each deformed sample, one for the texture measurement and another for GND assessment. The GND scans were performed with a step size of ~ 0.30 μm on average for all deformed samples with a slow data acquisition rate of around ~ 10 frames per second (fpc) or even lower. The EBSD patterns for texture measurements were acquired at a coarser step size, as compared to the GND scans, and acquisition speed of ~20 fpc. The orientation imaging maps were captured along the Transverse Direction (TD) plane of the samples. The Orientation Imaging Microscopy (OIM) data were captured at an accelerating voltage of 20 kV for sample A (virgin sample) however in the case of deformed samples a lower accelerating voltage of ~17–19 kV was maintained to capture patterns efficiently. The maintained tilting in the SEM chamber was 70° with respect to the EBSD detector. The OIM data were post-processed by the commercial OIM-TSL-8® software.

The EBSD scans were performed on hexagonal grids. The recorded Orientation Distribution Functions (ODFs) are presented for sections of $\varphi_2 = 45°$, $\varphi_2 = 65°$ and $\varphi_2 = 90°$, respectively. These three sections of the ODF reveal the important texture components and corresponding fibers, which tend to evolve during the thermo-mechanical history of Al alloys.

3. Results and discussion

3.1. Strain hardening

The phenomenon of strain hardening in the investigated samples A-I was analyzed by means of Vickers microindentation. The average hardness values were collected from the saturation zone of the ISE curve shown in Fig. 1 (see the dependence of hardness H_v over indentation depth h). The $H_v = f(h)$ dependence was investigated for each sample as the material response of the samples initiated by diamond-shaped indents (see the dependence of H_v over applied strain e in Fig. 1). In Fig. 1, the average hardness values are plotted against equivalent strain (e), which was calculated by the flow line modelling [29,30] in order to take accountability of localized shear components in total e for the subsurface under investigation.

The hardness values from the indentation load of 10gf, 25gf, 50gf, 100gf, 200gf, 300 gf, and 500gf have been plotted with respect to indentation depth h of the corresponding load for sample B (see Fig. 1). Other deformed samples reveal qualitatively similar $H_v = f(h)$ dependencies. Fig. 1 shows that for lower loads the Vickers hardness associated with the diamond-shaped indent is high, however, the H_v values tend to saturate from the load of 100gf. The characteristic

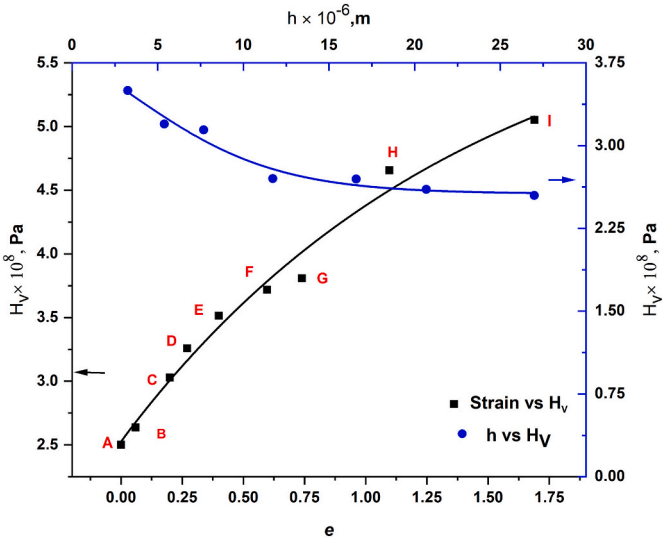

Fig. 1. Change in average microhardness as a function of indentation depth h for sample B (blue round-shaped symbols) and equivalent strain for samples A-I (black square-shaped symbols). (For interpretation of the references to colour in this figure legend, the reader is referred to the web version of this article.)

behavior in microhardness with applied load is known as the indentation size effect [27,31]. To eliminate the jump in measured data due to the ISE effect, the H_v values were taken from the range of 100gf to 500gf in the current work. In Fig. 1, the average hardness values from 100gf to 500gf are likewise represented as a function of strain for the investigated samples A-I. This dependence gives straightforward evidence of an increase in hardness in the samples from the virgin state of the material (Sample A) to the sample imparting the highest deformation level of 76% (Sample I). The steep change in hardness, in this case, can be correlated to the phenomenon of work hardening since one can notice a steady increase in the equivalent strain for deformed samples. To escalate numerous factors, responsible for work hardening, further experimental investigation has been performed and described below.

3.2. Orientation imaging microscopy (OIM) materials characterization

To capture the morphology of microstructural changes, orientation imaging contrast microscopy has been adopted, which reveals not only the change in grain structure but also the development of orientation gradients with the increase in deformation level. The latter can verify the evolution of the dislocation substructure. Figs. 2 and 3 show the KAM and Image Quality (IQ) maps superimposed with the Inverse Pole Figure (IPF) maps for the deformed samples B—I. The measurements were recorded with an average step size of 0.3 μm and a very slow scanning rate, which lasted from 12 to18 hours per sample to collect relevant information efficiently. The KAM maps are represented for the misorientation angle $0° \leq \theta \leq 5°$. The misorientations exceeding this range are dropped to avoid any artificial impact from the neighboring Grain Boundaries (GB), which makes it coherent for qualitative analysis of the dislocation density [32].

Figs. 2 and 3 show the change in the distribution of misorientation angle around High Angle Grain Boundaries (HAGB), as well as depict the phenomenon of grain fragmentation and formation of dislocation substructure in the samples as the straining level increases. In Fig. 2, sample B (5.3% deformed) shows localization of orientation gradients at the HAGB which is indicative of accumulation of GNDs. On the other hand, for sample C (15.8% deformed) the distribution of misorientation is found to be relatively homogeneous throughout the GB, accounting for uniform dislocation statistics, although regions of the lower density of geometrically necessary defects at the grain interior can be noticed. In some grains of sample C, a dislocation substructure (in the form of cells)

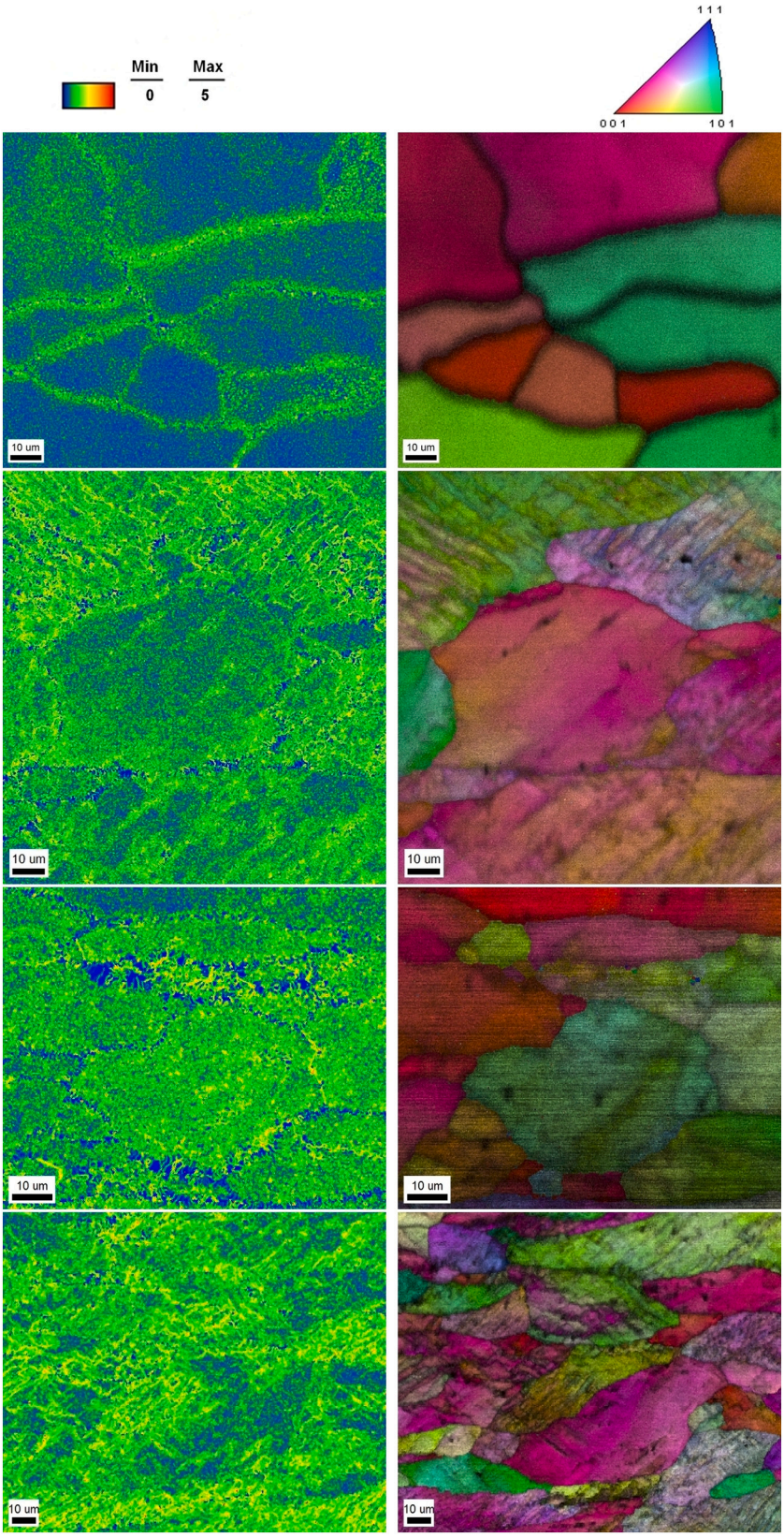

Fig. 2. KAM and IQ + IPF maps for deformed materials A-E: a) Sample B, b) Sample C, c) Sample D and d) Sample E. The KAM maps were calculated for the 1st neighbor and 5° upper threshold.

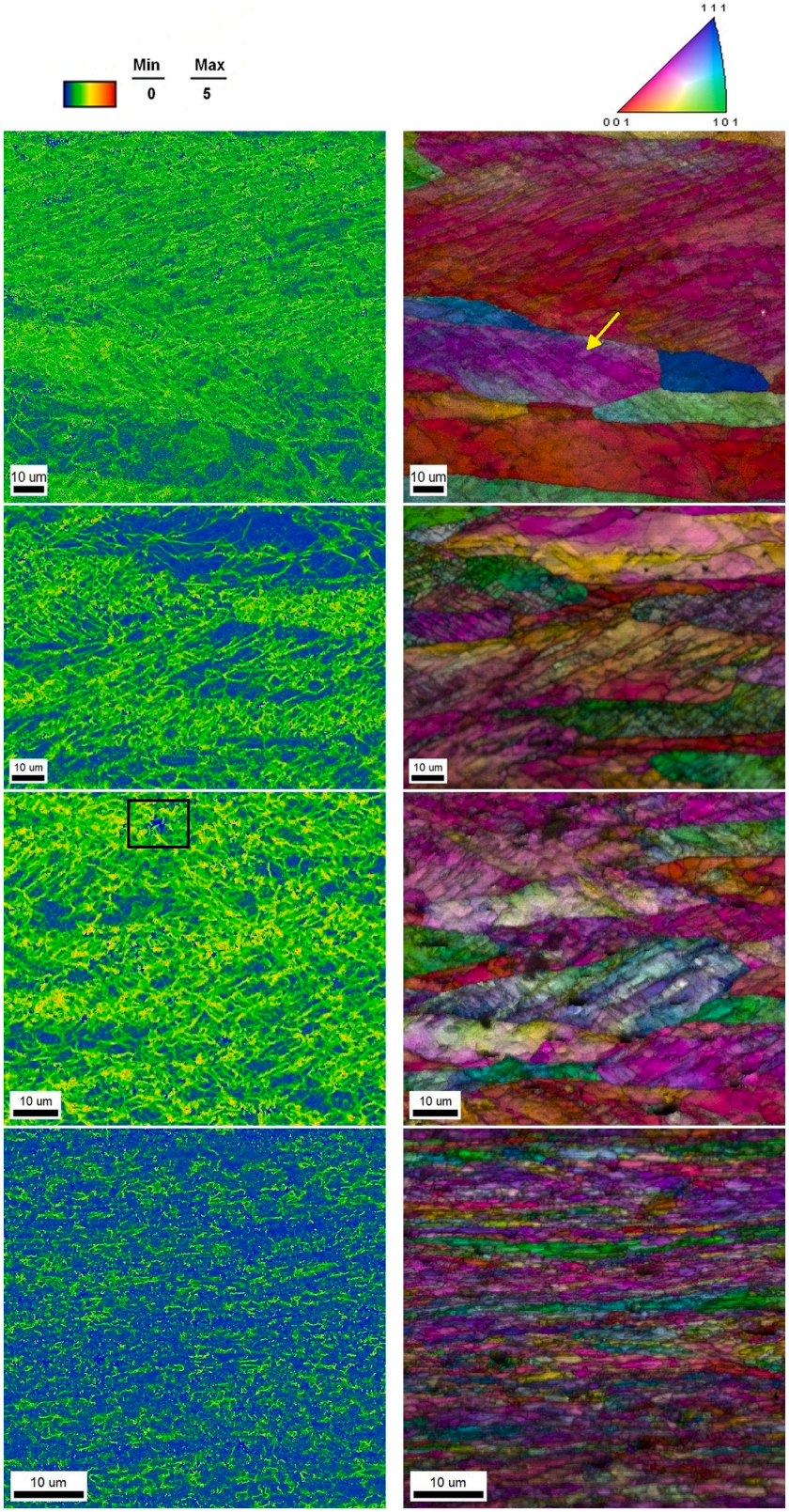

Fig. 3. KAM and IQ + IPF maps of deformed materials F-I: a) Sample F, b) Sample G, c) Sample H, d) Sample I. The KAM maps were calculated for the 1st neighbor and 5° upper threshold.

has been recorded to evolve at a region of dislocation accumulation. Similarly, for sample D (21.1% deformed) overall increase in average misorientation from the kernel can be identified within the grain but a minimum value of θ at the grain boundary has been observed. In samples B—D the formation of cells is not prominent although the GNDs tend to arrange themselves in the vicinity of the HAGBs. However, for samples F—I (Fig. 3) the evolution of complex dislocation structure is assisted by numerous dislocation subboundaries.

As indicated in literature sources [1,33,34], The process of grain subdivision can be considered as an indicator of an increase in dislocation density as the result of a higher straining level (as well as work hardening). In the present case, the IQ+ IPF maps of Figs. 2 and 3 reveal the formation of dislocation sub-structure with the formation of dislocation cells in the samples (marked by a yellow arrow). The comparison between the KAM and IQ+ IPF maps for samples indicates that for the zones of dense dislocation accumulation, the process of dislocation cell formation is intensive.

The evolution of dislocations is characterized by dislocation hot zones (regions of high dislocation concentration) for the reduction levels above 29%. In the case of sample H (60% deformed), the combined image quality-IPF map reveals the existence of particles, when the respective KAM shows an accumulation of dislocations around the particles (marked with a black box). The result of grain refinement is found to be quite intense in the case of sample I (76% deformed) while the size of dislocation cells also observed to be reduced strongly with an increase of straining level. The dislocations are found to be localized around the fine dislocation cells in sample I, which makes it difficult to capture a visible accountability of KAM misorientation. The recorded data provide evidence for the fact that the work hardening, phenomenon of grain refinement, and the evolution of dislocation structure with straining level are tightly interconnected processes. To observe the effect of the above-mentioned factors on crystallographic texture, EBSD scans for texture measurement were performed for the respective samples.

The ODFs presented in Figs. 4 and 5, reveal the evolution of crystallographic texture in the investigated materials A-I. For sample A, the overall texture is dominated by the Cube component {001} ⟨100⟩, demonstrating the annealed state of the material, while the traces of Brass orientation can also be found. The {011} ⟨112⟩ component typically appears in cold rolled Al alloys [35], but in the current case the material was fully recrystallized, and this orientation can be considered as a retained rolling texture component. From sample B onwards, the rotation of the recrystallization texture components towards the rolling texture components is observed. For sample F, the evolution of β- fiber is recorded, which connects the Copper {112} ⟨111⟩, Brass {011} <112> and S-component {123} <9 15 11 > in Euler space, characterizing enhancement of deformation textures [35,36]. However, the existence of recrystallization texture component i.e., Cube component and weak Goss in case of samples E and G; can be observed in ODF maps till 60% rolling reduction of the material. On the other hand, sample I shows only rolling texture components, i.e., the β- fiber. The intensity of ODF has been found to drop as the straining level increases and this is due to the fact that the volume fraction of the initially strong cube component

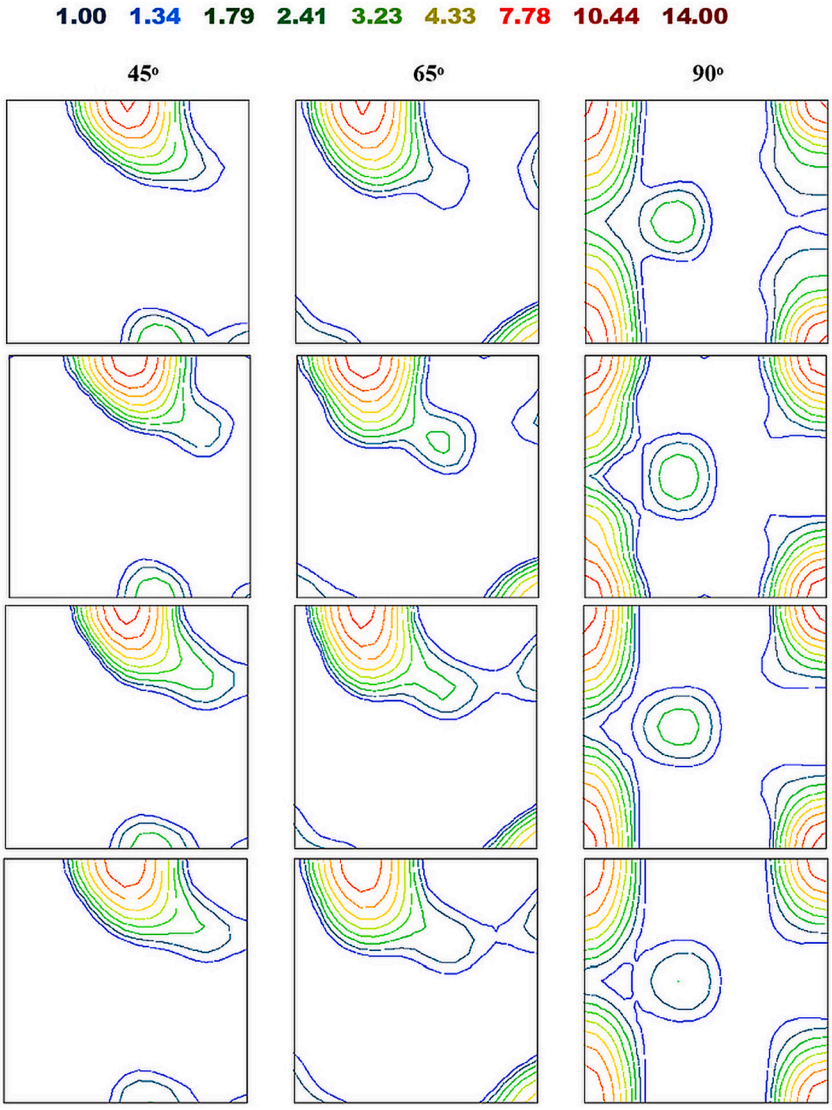

Fig. 4. Three section ODF map for sample: a) annealed undeformed sample A, b) 5.3% deformed, $ODF_{max} = 13.15$; c) 15.8% deformed, $ODF_{max} = 12.12$; d) 21.1% deformed, $ODF_{max} = 8.73$.

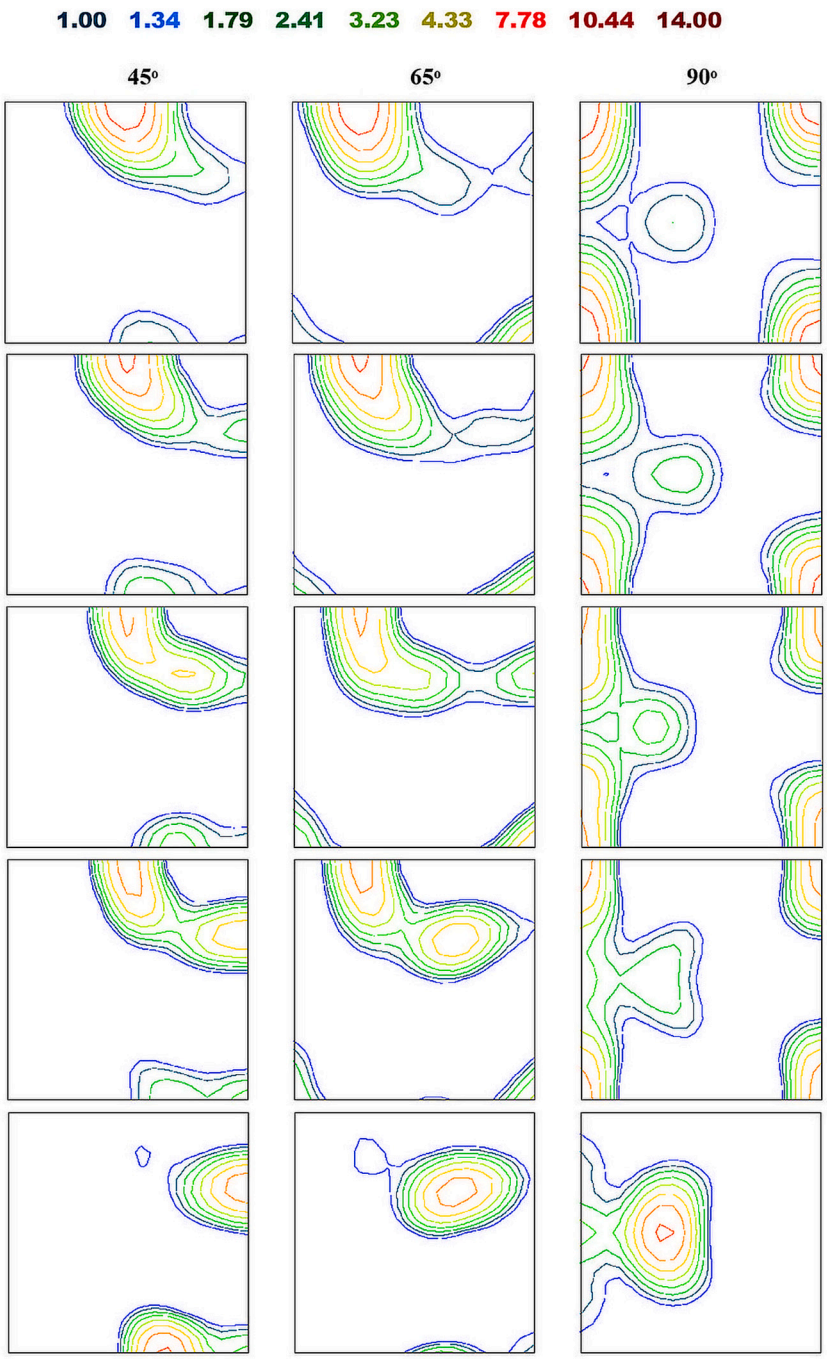

Fig. 5. Three section ODF map for sample: a) 28.9% deformed, $ODF_{max} = 10.23$; b) 40% deformed, $ODF_{max} = 8.48$; c) 46.8% deformed sample, $ODF_{max} = 6.41$; d) 60% deformed, $ODF_{max} = 6.86$; e) 76% deformed, $ODF_{max} = 8.22$.

tends to decrease with the increase of rolling reduction. It is obvious from Figs. 4 and 5 that the intensity of rolling texture components tends to intensify with the rise of strain.

From the OIM scans, other important microstructural parameters such as grain size and Taylor factor (*M)* were calculated. While calculating the respective value of *M* for the samples, the components of the strain velocity gradient tensor were calculated using flow line modelling [29,30] to capture the effect of different strain profiles that might arise during the process of cold rolling [37]. Table 1 shows continuous grain fragmentation with the increase of equivalent strain, while the values of Taylor factor reveal a tendency towards the increase since the values of *M* are higher for the deformation texture components as compared to recrystallization counterparts such as Cube or {011} <100> Goss

Table 1
Values of strain *e*, the average value of grain size, Taylor factor (*M*) and approximated cell size for samples A-I based on data reported in Ref. [36].

Sample	*e*	Grain size (μm)	Taylor factor, M	Cell size (μm)
A	0	74.8	3.146	–
B	0.06	70	3.097	~2 or larger
C	0.20	67.865	3.113	~1.1 or larger
D	0.27	63.305	3.057	0.98
E	0.40	58.07	3.117	0.86
F	0.59	50.83	3.117	0.76
G	0.74	54.66	3.143	0.70
H	1.09	29.20	3.162	0.597
I	1.69	25.1	3.216	0.49

orientations.

The calculated values of *M* in Table 1 are used for the computation of dislocation density by Eq. (1). The subcell sizes for all deformed samples were approximated from the experimental data, reported in Ref. [38] to obtain a better accountability of quantitative assessment of dislocation density [39]. It should be noted here that the cell sizes for the straining levels (below 0.27) are rather indicative since the approximation of the exact subcell sizes from the experimental evidence [38] is complicated by the fact that the cell size tends to approach infinity in size (large) at low strains. In practice, this means that the subcells are either not formed after the small reductions or their sizes are relatively large, implying that dislocations can travel distances comparable to the average grain size.

Fig. 6 shows an increase in KAM angle with the equivalent strain calculated by the Flow Line Model for the subsurface regions of deformed samples B—I. It is obvious that the extent of increment in KAM tends to slow down after $e \sim 0.74$. The KAM angle is a measure of the local plastic strain in grains and the increase in KAM value suggests both the existence of strained grains and a greater concentration of geometrically necessary dislocations. In case of sample I, as it coexists with the highest straining level and experiences intense grain fragmentation out of all the samples, the KAM map reveals the highest kernel average misorientation angle.

3.3. Evolution of dislocations

3.3.1. Assessment of dislocation density in deformed materials

To further extend the investigation of the deformation mechanism and the evolution of work hardening in Al 1050, dislocation density (ρ) for the samples B—I were calculated using Eq. (1) with the Taylor factors listed in Table 1. The Burgers vector *b* and shear modulus *G* are known for Aluminum: $b = 0.2863$ nm, and $G = 26.5$ GPa. The value of geometric constant α for the population of edge and screw dislocations can be calculated using the formula given below [1]:

$$\alpha \cong \frac{(1-0.5\nu)}{4\pi(1-\nu)} ln\left(\frac{\Lambda}{b}\right) \tag{5}$$

Where, Λ is the mean free path of dislocations, which is inversely proportional to the dislocation density (can be computed by Eq. (3) for various strain increments; the dependence of α over equivalent strain is well elaborated elsewhere [5]), ν is a Poisson ratio ($\nu = 0.35$ for Al).

Along with the above-mentioned factors, considering the microhardness values (H_V) obtained from the Vickers microhardness test, the dislocation density for all deformed samples was estimated by employing Eq. (1). The values of ρ for samples B—I are presented in Table 2 as well as in Fig. 7. As follows from Fig. 7, the dislocation density of the material increases with the increase in deformation level. The minimum value of $\rho = 4.08 \times 10^{13}$ m^{-2} corresponds to sample B, while the highest value of dislocation density 2.94×10^{14} m^{-2} is observed in sample I, which imparts the highest deformation and hardness value out of all of samples under investigation. The trend of increase in ρ values can be correlated to the evolution of work hardening (see Fig. 1).

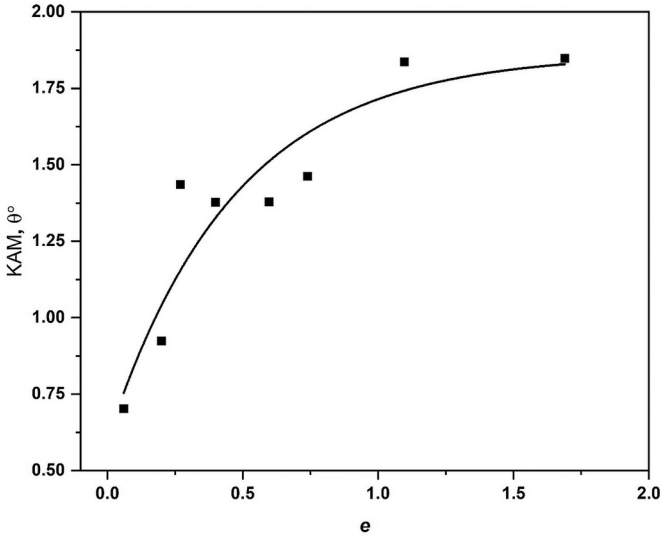

Fig. 6. Variation of KAM misorientation angle with equivalent strain *e*.

Apart from experimental evidence, the dislocation density of deformed samples was likewise approximated by the K-E and simplified K-E models (see Eqs. 2(a), 2(b), and 3). For the calculation of mobile and forest dislocations by the Kubin-Estrin numerical approach, the model parameters C_1, C_2, C_3, and C_4 are determined for pure aluminum deformed at room temperature and given as follows: $C_1 = 2.33 \times 10^{14}$ m^{-2}, $C_2 = 1.1$, $C_3 = 4 \times 10^5$ m^{-1}, $C_4 = 1.2$ [9]. The K–E technique requires defining the initial ρ, which corresponds to the unstrained material and was approximated by the ρ ($\varepsilon = 0$) $= 10^{10}$ m^{-2}, while the fraction of the mobile and forest dislocations was defined as $\rho_m = \rho_f = \rho(\varepsilon = 0)/2$ [8,9]. On the other hand, for the simplified K- E method, the associated model parameters for pure Al are given by $C_1 = 2.33 \times 10^{14}$ m^{-2} and $C_4 = 1.15$ [9]. The dislocation density calculated by both numerical models is presented in Fig. 7, along with ρ values obtained from the indentation technique for all deformed samples. It is obvious that the dislocation density values obtained by numerical models employed are in good agreement with the experimental results obtained from the indentation. It has been observed that at lower straining levels (up to ~0.5) the numerical methods seem to underestimate the dislocation density, but it should be mentioned that the indentation might induce the development of additional dislocations in the vicinity of the indent and therefore can locally increase the dislocation density. This effect will be more prominent for the sheets deformed to a lower extent, i.e., when the material contains only a limited number of dislocations. Moreover, evaluation of dislocation density in the deformation-free material A provides a value of ~10^{13} m^{-2}, which is evidently a significantly overestimated value of ρ for the fully recrystallized material. Given this, the assessment of dislocation density by Eq. (1) for very low strains (or fully recrystallized materials) should be treated with particular care.

3.3.2. GND assessment from the OIM

It is important to understand the contribution of dislocation density components (geometrical and statistical) in increasing hardness values for respective deformed state. For the calculation of GND density, the modified KAM technique has been considered which is also known as Kamaya's technique [24,25] and employs Eq. (4) in the following modified form:

$$\rho_{GND} = \frac{k}{b} \times \frac{d\theta}{ds} \tag{6}$$

As compared to Eq. (4), the value of $< \theta >_s$ has been replaced by its gradient ($\frac{d\theta}{ds}$) to reduce the noise parameters and the effect of step size in the calculation of GND density [24]. The value of constant *k* is defined separately for the substructures built of arrays of edge and screw

Table 2
Assessment of GND and SSD in total dislocation density with the change of *e*.

Sample	Total dislocation density (ρ)(m^{-2})	ρ_{GND} (Method 2, Experimental) density (m^{-2})	ρ_{SSD} density (m^{-2})
B	4.08×10^{13}	1.28×10^{13}	2.80×10^{13}
C	7.00×10^{13}	2.43×10^{13}	4.57×10^{13}
D	9.07×10^{13}	4.21×10^{13}	4.86×10^{13}
E	1.11×10^{14}	5.32×10^{13}	5.79×10^{13}
F	1.37×10^{14}	6.92×10^{13}	6.76×10^{13}
G	1.47×10^{14}	7.46×10^{13}	7.26×10^{13}
H	2.39×10^{14}	9.89×10^{13}	1.40×10^{14}
I	2.94×10^{14}	1.35×10^{14}	1.58×10^{14}

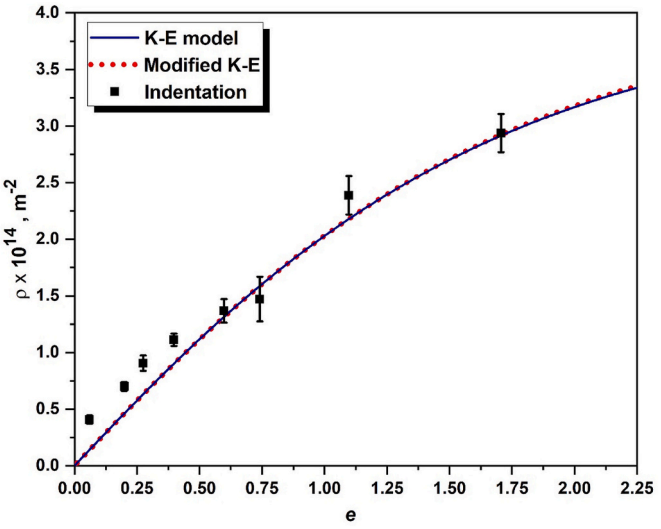

Fig. 7. Evolution of dislocation density in samples B—I as computed from the indentation measurements and two numerical models employed [5,7–11].

dislocations: *k(edge)* = 1 and *k(screw)* = 2. In the present study, *k*=1.5 has been chosen in view of the fact that the overall dislocation structure is a combined effect of both edge and screw dislocations [40].

Fig. 8 depicts a linear dependency of kernel average misorientation angle over the step size (kernel radius). The GND calculated by the simplified method of Eq. (4) shows a strong dependency of ρ_{GND} on kernel radius as the amount of GND tends to decrease sharply with the increase of step size. On the other hand, it must be noted that the error associated with misorientation estimation in 2-D EBSD technique is $\theta < 2^\circ$ [41]. To avoid this noise, as well as a strong kernel radius dependency and uncertainty in choosing the GND value corresponding to a particular neighbor rank of the kernel, Kamaya's method [24,25] of GND calculation from KAM angle has been chosen for this study. According to this technique, the value of the $d\theta/ds$ was derived from the dependence of the KAM angle on kernel radius, which enabled the calculation of GND density using Eq. (6). The GND values estimated are authentic, not only for the reason that the data were collected with a confidence index higher than 0.1 but also because the GND scans were performed over areas as large as ~ 0.5 mm^2 for all deformed samples. The maximum misorientation was set to 5° in order to avoid the effect of orientation error near the grain boundary [23]. The GND densities calculated by Eq. (6) are presented in Fig. 10. A sharp rise in the GND density is recorded with an increase in plastic strain from 0 to 0.5 (sample B, 3.04 × 10^{12} m^{-2} to sample D, 5.01 × 10^{13} m^{-2}), and afterward, the amount of GNDs tends to level off, reaching the highest value of 1.54 × 10^{14} m^{-2} (sample I). This trend can be correlated with the qualitative observations of KAM evolution, presented in Figs. 2 and 3.

Alternatively, to the above-presented method, the amount of GNDs can be calculated by the method developed by Field et al. [42] (implemented in the TSL OIM software). This algorithm involves the computation of misorientation between the neighboring points and the assessment of Nye's tensor [20] components. The dislocation density tensor of Nye consists of the tensor ω_{ij} that correlates the effect of dislocations in the lattice with Burger's vector *i* and the dislocation line vector *j*. The tensor ωij consists of 9 components of lattice curvature terms that quantify the net dislocation flux through a unit area [20,21,42]. In the current investigation, we have performed computations based on the algorithm, embedded in the TSL OIM-8 software that calculates the GND using Nye's dislocation tensor by taking into account the presence of both pure edge and pure screw dislocations [42]. While calculating the GNDs, the maximum possible GND value was set in a way that it was equal to the total dislocation density (can be estimated either experimentally or by Eq. (3)), as GND cannot exceed the total amount of ρ. On the other hand, to understand the dependency of GND values on the step size, two different procedures of GND calculations were employed: i) calculation of GND density with a fixed step size of 0.6 μm, independently of the degree of straining, ii) estimation of GNDs with a step size comparable to the sub-cell size, which tend to evolve during deformation (see Table 1 and Figs. 9 and 10 for details). In both cases, the calculation was carried out for the maximum misorientation of 5°. The GND values obtained for a fixed step size of 0.6 μm are represented in Fig. 10. While calculating the amount of GNDs by employing the algorithm (ii), it has been observed that the cells are not formed at small strains (5%, sample B) and the dislocations are trapped by the grain boundaries (see Fig. 2). At higher strains (15–21%, samples C and D), the

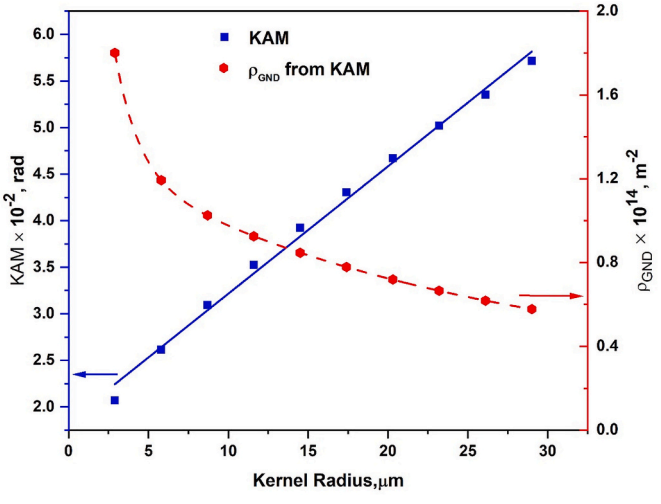

Fig. 8. GND and KAM evolution in 1050 Al alloy, deformed with 46.8% thickness reduction (sample G): a) average KAM angle in radians (blue square-shaped symbols) with a cut-off threshold of 5° as a function of kernel radius (1st to 10th neighbor). b) GND (red symbols), calculated from each KAM angle using Eq. (4), as a function of kernel radius. (For interpretation of the references to colour in this figure legend, the reader is referred to the web version of this article.)

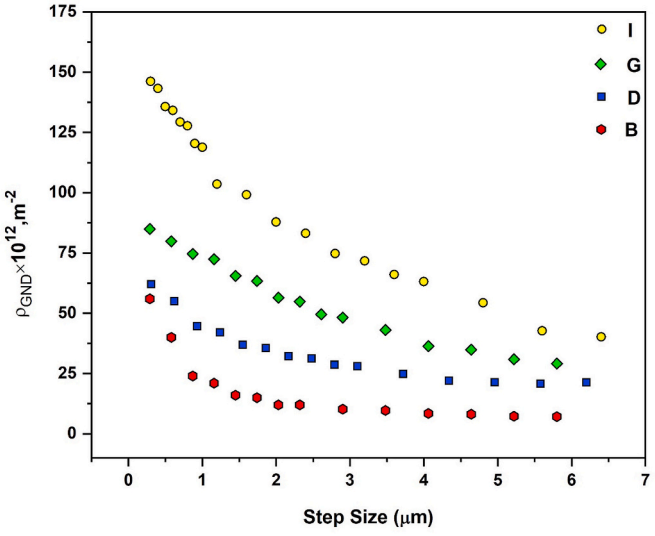

Fig. 9. GND dislocation densities calculated for selected samples, subjected to low (samples B and D, *e* = 0.06 and *e* = 0.27), intermediate (sample G, *e* = 0.74) and high (sample I, *e* = 1.69) rolling reductions by TSL-IOM software as a function of step size. The algorithm of GND calculations implemented in the TSL-IOM software is based on the computation of Nye's tensor components and described in Refs. [42].

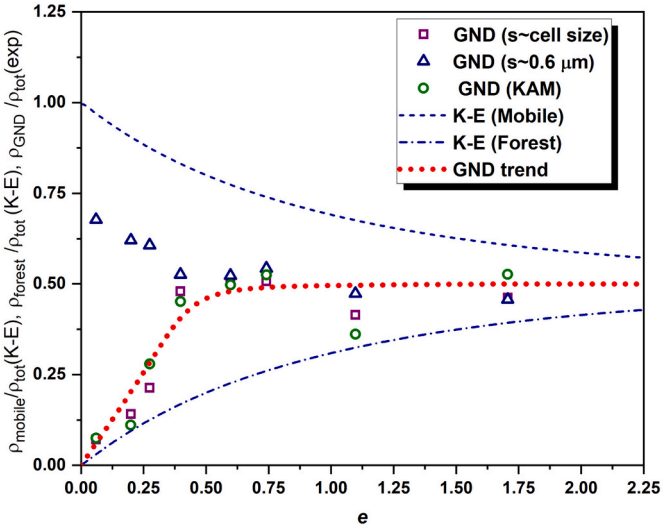

Fig. 10. Evolution of GND in 1050 Al alloy as defined by KAM and Nye's tensor [42] technique employed for different step sizes. The red dotted line reveals the GND trend. (For interpretation of the references to colour in this figure legend, the reader is referred to the web version of this article.)

distribution of GNDs is more homogeneous within the grain, compared to sample B, but the formation of the cells is still not prominent. Hence, taking this event into account, the GND values for samples B and D were calculated for step sizes ranging between 0.3 and 6 μm (Fig. 9). Fig. 9 shows a sharp exponential decay in GND values as the step size increases. The high value of GND at a lower step size (~ 0.5 μm) corresponds to the noise associated with a very small step size [22]. Taking into account the fact that there is no significant cell formation in samples B—D, the values of ρ_{GND} were collected from the saturation zones (see Fig. 9), observed for the step sizes exceeding 2 μm. In the same manner, the GND densities over a broad range of step sizes are plotted in Fig. 9 for samples subjected to higher deformation i.e., G and I. In these materials, the sub-cell formation was intense as per Fig. 3. The GND values of samples G and I tend to saturate earlier with respect to the step size, as compared to samples B and D (cf. Fig. 9). In the case of samples G and I (Fig. 9), the GND value corresponding to the sub-cell size belongs to the saturation zone of ρ_{GND} vs step size dependence. With the multiplication of dislocations after a reduction of 28.9%, the cell formation is observed in the majority of grains, hence, for samples E – I the step size comparable to the sub-cell size was considered in the corresponding GND calculations.

The GND values (ρ_{GND}) calculated by Eq. (6) (method 1), and Nye's tensor with step size comparable to sub-cell size (TSL OIM software [42], method 2) are plotted in Fig. 10 as a variable function of forest and mobile dislocations calculated by Eqs. 2(a) and 2(b). It is obvious that while calculating the GNDs using Nye's tensor with a fixed step size of 0.6 μm (TSL OIM software [42], method 3), the fraction of GND dislocations to the total ones (ρ_{GND}/ρ_{tot}) is significantly higher for less strained samples (sample B—D), compared to counterparts calculated with the Kamaya's method or step size *s* (method 2), comparable to the cell size (see Table 1). At the straining levels exceeding the value of ~0.5, the fraction of ρ_{GND}/ρ_{tot} tends to provide comparable values for all three methods.

4. Discussion

Analyzing the mesoscopic changes in the investigated materials A-I (Figs. 2 and 3), it should be noted that the evolution of kernel average misorientation is attributed to the GND density (see Eq. (6)) as the maximum misorientation of 5° corresponds to dislocation structure evolution only in the mentioned range. These dislocations, accommodating geometric factors and associated with the lattice deformation, re-arrange themselves to minimize the total energy state forming dislocation cell structure bounded by Dense Dislocation Walls (DDW) [43]. As the strain increases, the dislocation cells form dislocation subboundaries, which eventually turn into high-angle grain boundaries, resulting in grain refinement/fragmentation. As reported in the literature [43], the refinement process continues within the new grains, but the fragmentation of the sub-grains will stop as the rate of dislocation annihilation became equal to the rate of dislocation multiplication. It has been stated [44] that the formation of dislocation cells is initiated by easily intersecting glide planes which confine zones of very low dislocation density (can be seen in Fig. 3). The rearrangement of GNDs further increases the total amount of dislocations. This process continues as the deformation level increases imparting hardness to the material as a result of grain refinement as per Hall- Petch strengthening relation [45]. The latter initiates the pilling up of dislocations at the grain boundaries especially at the initial stage of the work hardening [44]. On the other hand, the increase in KAM angle with equivalent strain suggests that additional dislocation generation is required to maintain a structural homogeneity of the samples, due to strain incompatibility in the grain assembly. This is satisfied by the formation of GNDs. The described effect becomes more prominent with a decrease in average grain size and this phenomenon can be correlated to Ashby's simplified grain boundary hardening model [13]. Hence, a combination of KAM maps and image quality IPF maps are effective tools enabling qualitative analysis of dislocation evolution.

Taking into account the crystallographic aspect of microstructure evolution, it should be noted that the polycrystalline aggregate consists of grains of various orientations (see Figs. 4 and 5) and therefore the macroscopic deformation is accommodated differently in individual crystals. The incompatibility of deformation in the grain assembly is caused by the variety of Schmid/Taylor factors which are responsible for the activation of corresponding slip systems in differently oriented grains. The heterogeneous nature of deformation at lower strains is compensated by the evolution of GNDs on the grain boundaries, which is well explained by the strain compatibility and stress equilibrium theory [45,46]. Considering strain compatibility and stress equilibrium at the GBs in the crystal plasticity approaches such as the advanced LAMEL model [47,48] leads to accurate prediction of texture evolution during plastic deformation [30,49,50]. At advanced stages of deformation, the efficient accommodation of deformation is accompanied by the substructure evolution and grain fragmentation [14–16,18]. The evolution of subcells with characteristic sizes (see Table 1) is a function of straining level, however, the lower bound for the subcell size is ~0.5 μm, and this size is characteristic for severe straining levels ($e > 2$).

Since the fixed step size of EBSD measurements (0.6 μm) employed for GND calculation (see Fig. 10) provides an evolutionary pattern reverse to those provided by the other two methods employed (method 1 and 2), it is important to clarify the nature of dislocation evolution. In view of this, the fraction of mobile and forest dislocations was calculated by the K-E model [7] (see Fig. 10). Assuming that the fraction of both counterparts was equal prior to deformation, one can clearly notice that the portion of mobile dislocations is dominating at the very early stages of deformation, whereas the number of forest dislocations tends to increase as the deformation proceeds. At larger reduction levels ($e > 0.5$), the fraction of mobile and forest dislocations seems to be equibalanced (see red dotted line in Fig. 10). As Figs. 2 and 3 suggest, the majority of dislocations are located in the close vicinity of grain boundaries (GBs) at low strains ($e < 0.5$), while at higher straining levels the dislocations are arranged in the form of dislocation walls in grain interior, accounting for orientation gradients. Since the GNDs in the neighborhood of GBs are blocked, they can be assimilated with the SSD counterparts. In fact, the amount of SSDs prevails over the GNDs since the local misorientations in the grain interior are rather low at small strains. The GNDs seem to contribute more to hardening at higher strains (see Fig. 3). The observed evolutionary pattern is consistent with the work of Hansen and Huang

[51], where the substructures evolved in pure Al after different tensile deformations were analyzed by TEM. In this work [51], the contribution of the so-called crystallographic dislocation boundaries, defining cell blocks (associated with the GNDs), to the total dislocation density is lower compared to SSDs for the tensile deformations ranging between 5% and 34%. In the present case, the evolution of GNDs as calculated by methods 1 and 2 provides a physically sound evolutionary trend, which is consistent with the results reported elsewhere [51].

Investigated the substructure evolution, Lehto [52] has reported the existence of misorientations $0.4^\circ \leq \Psi \leq 1^\circ$ between Dense Dislocation Walls. This concept enables rough estimation of the upper and lower limits of GND density only for materials subjected to higher deformation degree, i.e., when the formation of dislocation cells is highly probable. The rough approximation of the upper and lower limits for GND density can be done by using the following equation:

$$\rho_{GND} = \frac{1.5 \times \Psi}{bl} \tag{7}$$

Where, Ψ is 0.4° and 1° for the lower and upper bounds and l is a cell size.

Eq. (7) has been reformulated using Eq. (4) by redefining s as approximate cell size [38], associated with corresponding strain e, and k=1.5 [40]. Figs. 3 and 4 indicate that the distinct process of dislocation cell formation starts only after moderate straining, i.e., $e \sim 0.4$ (sample E).

Let's consider three cases when the material is subjected to the moderate ($e = 0.4$), high ($e = 1.7$), and severe ($e = 3$) deformation:

Case 1: $e \geq 0.4$, the misorientation between DDWs is low, $\Psi = 0.4^\circ$. The approximated GND density by Eq. (7) is: $\rho_{GND} = 4.25 \times 10^{13}$ m^{-2} (cell size corresponding to $e = 0.4$ is ~0.86 μm, see Table 1). Since the ρ_{tot}(K-E) $= 9 \times 10^{13}$ m^{-2} for this strain, ρ_{GND}/ρ_{tot}(K-E) = 0.47.

Case 2: $e \geq 1.1$, $\Psi = 0.7^\circ$. The approximated GND density by Eq. (7) is: $\rho_{GND} = 1.07 \times 10^{14}$ m^{-2} (cell size corresponding to $e = 1.1$ is ~0.6 μm, see Table 1). Since the ρ_{tot}(K-E) $= 2.18 \times 10^{14}$ m^{-2} for this strain, ρ_{GND}/ρ_{tot}(K-E) = 0.49.

Case 3: $e \geq 3$, $\Psi = 1^\circ$. The approximated GND density by Eq. (7) is: $\rho_{GND} = 1.83 \times 10^{14}$ m^{-2} (we must take into consideration the fact that the reduction in cell size tends to saturate at ~0.5 μm for highly deformed materials). Since the ρ_{tot}(K-E) $= 3.68 \times 10^{14}$ m^{-2} for this strain, ρ_{GND}/ρ_{tot}(K-E) = 0.5.

In all above cases ρ_{GND}/ρ_{tot} (K-E) ≈ 0.5, which follows the trend line of ρ_{GND}/ρ_{tot} obtained from the experimental values (red dotted line of Fig. 10). The present analysis provides experimental validity to the GND approximation approach, described by Eq. (7). Since the contribution of GNDs to the total dislocation density is ~ 50% for straining levels ≥40%, it is possible to make the reverse calculations of workable step size for experimental estimation of GND by EBSD technique with the help of K-E model and approximation expressed by Eq. (7).

The experimentally measured total dislocation density (ρ), ρ_{GND} assessed by TSL OIM software with step size comparable to sub-cell size (method 2) and corresponding SSD (ρ_{SSD}) are presented in Table 2. The amount of statistically stored dislocations was computed as a difference between the total dislocation density (estimated by Eq. (1)) and the corresponding amount of GNDs. The recorded data show that there is a rise in the amount of both GNDs and SSDs as the deformation level rises. On the other hand, it must be noted that the overall dislocation density is dominated by the accumulation of SSDs at lower straining levels.

Analysis of both Table 2 and Fig. 2 suggests that there is an abrupt increase in the overall dislocation density during the initial stages of straining and similar tendency has been observed in the case of generation of GNDs. The mobile GNDs at very low strains are quickly trapped by the grain boundaries as the deformation proceeds, converting them to forest dislocations in the investigated 1050 Al alloy. The rate of increase in dislocation density seems to slow down on reaching a certain straining level of strain ($e \sim 0.4$). When the reduction level approaches 30%, nearly 50% of the GNDs became mobile, while others are trapped by the dislocation walls or other obstacles. Further deformation of the investigated 1050 Al alloy shows a similar morphological tendency in the accumulation of GNDs. The increment in both GND and SSD density is recorded with an increase in e. This trend is supported by the investigations [18,52,53], which report that the accumulation of SSDs rises by random trapping of other SSDs and GNDs as plastic strain increases. Our investigation leads to the conclusive remark that the overall dislocation density is dominated by the density of SSDs for less strained samples, suggesting that the SSDs are primarily responsible for hardening in materials with a high stacking fault energy such as 1050 Al. Both Fig. 10 and Table 2 depict that the fraction of GNDs and SSDs are nearly equal as the level of straining increases ($e > 0.5$) and hence both counterparts contribute almost proportionally to the strain hardening. As the dislocation density tends to saturate after the particular straining level, the majority of one-dimensional defects will become forest due to mutual interaction between the dislocations, directing the density of GNDs towards the saturation level.

Estimation of dislocation density is important since the phenomenon of recovery, recrystallization and grain growth are driven by the amount of linear defects present in the deformed material [1]. The driving force for recrystallization is associated with the stored energy (E_D) of the existing dislocations, which can be calculated as following [1]:

$$E_D = \alpha \rho G b^2 \tag{8}$$

In Eq. (8), the geometric constant α is calculated by Eq. (5), while the dislocation density is estimated either experimentally or by the numerical approaches mentioned above [7,8].

The calculated stored energies for experimentally obtained dislocation densities of materials B—I are presented in Fig. 11. The driving force of recrystallization tend to change between the 5.6 kJ/m^3 and 343.3 kJ/m^3 for samples subjected to rolling reduction ranging between 5.3 and 76%. It is obvious that with an increase of deformation level, the dislocation densities of investigated materials rise (see Fig. 7) and the E_D values follow the same evolutionary pattern (see Figs. 7 and 11). The estimated stored energies by employing results of indentation or numerical approximations provide values comparable to ones reported elsewhere ($E_D \sim 10^4$–10^5 J/m^3) [10,54]. Taheri et al. [10] derived the deformation energy stored in a cold rolled Al by implementing various techniques such as TEM, EBSD, microindentation and Differential Scanning Calorimetry (DSC). The stored energy obtained by the DSC and

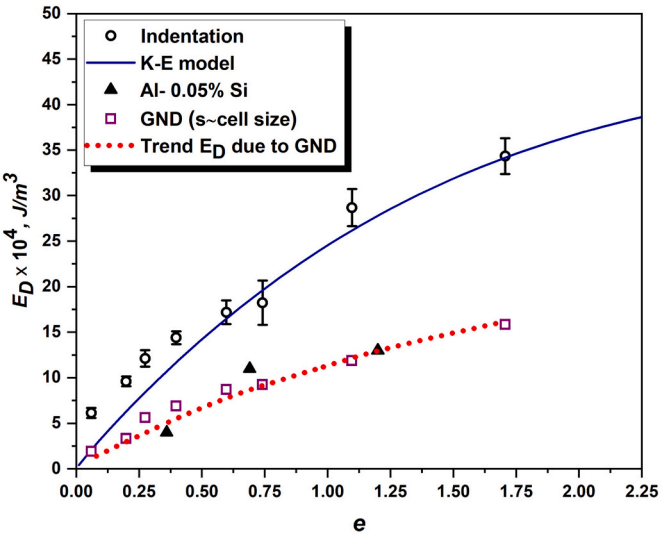

Fig. 11. Variation of stored energies as a function of equivalent strain e in 1050 Al alloy. The data for Al-0.05Si alloy are collected from elsewhere [54]. The red dotted line shows the trend of E_D due to GNDs. (For interpretation of the references to colour in this figure legend, the reader is referred to the web version of this article.)

microindentation showed a good agreement with each other, while the counterparts derived from EBSD and TEM were ~ 60% lower compared to the DSC/microhardness E_D values. The difference was attributed to the fact that EBSD/TEM can only measure the GNDs [10]. In the current investigation, the amount of GNDs was ~50% of the total dislocation density, which is in a good agreement with the work of Taheri [10]. In addition to this, Huang and Humphreys [54] have estimated the stored energy from EBSD measurements, taking into account the evolution of both substructure and misorientation in Al-0.05Si alloy. The results obtained in this work [54] are in a good agreement with the E_D values calculated exclusively for the GNDs of samples B—I (see Fig. 11). The dotted trendline of Fig. 11, which represents the change of stored energy with strain due the evolution of GNDs (estimated with a step size comparable to the cell size), clearly demonstrates that a significant amount of SSDs contribute to stored energy even at lower straining levels.

5. Conclusions

The process of work hardening in cold rolled 1050 Al alloy was investigated by means of microindentation, orientation imaging microscopy, and numerical approaches. The following conclusive remarks were withdrawn:

The total dislocation density estimated by indentation is well correlated with the numerical results obtained by employing Kubin-Estrin (K-E) and a simplified version of this model. The K-E model facilitates the estimation of mobile and forest dislocations, which enables understanding the partitioning of total dislocation density to geometrically necessary (GND) and statistically stored (SSD) counterparts.

Orientation Imaging Microscopy is a powerful tool for the assessment of GNDs in deformed materials. Choosing the appropriate step size is of crucial importance since both noises associated with the very fine step size, or miscalculated misorientation due to a coarse-stepped measurement affect the results of GND calculation. Kamaya's technique seems to be an effective approach for the estimation of geometrically necessary dislocations while performing the assessment of GNDs with a fixed step size does not necessarily lead to a physically sound result. The step size of scans, used for the GND analysis, should be comparable to the size of the subcell structure, which tends to evolve during deformation. The numerical approach applied for a rough estimation of GND density was found to be reliable, compared to the experimental method. Hence, with the help of the simplified K-E method and formulated GND approximation technique it is possible to study the deformed state of strained materials. These methods likewise enable determination of an appropriate step size for EBSD scans.

Results of our investigation suggest that the GNDs are trapped by grain boundaries and the total dislocation density is dominated by the density of SSDs at the early stages of deformation. As the strain exceeds the level of 0.5, the GNDs and SSDs nearly equally contribute to the strain hardening.

The calculated stored energies for various straining levels clearly demonstrate that the indentation technique reflects the contribution of both SSDs and GNDs, while the EBSD reveals the contribution of GNDs only.

Credit authorship contribution statement

Purnima Chakravarty: Conceptualization, Methodology, Data Curation, Investigation, Validation, Writing - original draft, Writing - review & editing, Visualization. **Gyula Pál**: Formal analysis, Methodology. **Jurij J. Sidor**: Conceptualization, Methodology, Visualization, Validation, Writing – original draft, Writing – review & editing, Investigation, Funding acquisition, Project administration, Supervision.

Data availability

The modelling results can be reproduced using the reported material parameters. The experimental data are available upon request by contact with the corresponding authors.

Declaration of Competing Interest

We declare no conflict of interests.

Data availability

Data will be made available on request.

Acknowledgements

Project no. TKP2021-NVA-29 has been implemented with the support provided by the Ministry of Innovation and Technology of Hungary from the National Research, Development and Innovation Fund, financed under the TKP2021-NVA funding scheme.

References

[1] F.J. Humphreys, G.S. Rohrer, A.D. Rollett, Recrystallization and Related Annealing Phenomena, Third edition, Elsevier, Amsterdam Oxford Cambridge, MA, 2017.
[2] T.W. Clyne, J.E. Campbell, Testing of the Plastic Deformation of Metals, 1st ed., Cambridge University Press, 2021 https://doi.org/10.1017/9781108943369.
[3] J. Gubicza, T. Ungár, Characterization of defect structures in nanocrystalline materials by X-ray line profile analysis, Z. Für Krist. - Cryst. Mater. 222 (11) (Nov. 2007) 567–579, https://doi.org/10.1524/zkri.2007.222.11.567.
[4] Y. Meng, X. Ju, X. Yang, The measurement of the dislocation density using TEM, Mater. Charact. 175 (May 2021), 111065, https://doi.org/10.1016/j.matchar.2021.111065.
[5] J.J. Sidor, P. Chakravarty, J. Gy Bátorfi, P. Nagy, Q. Xie, J. Gubicza, Assessment of dislocation density by various techniques in cold rolled 1050 aluminum alloy, Metals 11 (10) (Sep. 2021) 1571, https://doi.org/10.3390/met11101571.
[6] T. Berecz, P. Jenei, A. Csóré, J. Lábár, J. Gubicza, P.J. Szabó, Determination of dislocation density by electron backscatter diffraction and X-ray line profile analysis in ferrous lath martensite, Mater. Charact. 113 (Mar. 2016) 117–124, https://doi.org/10.1016/j.matchar.2015.11.014.
[7] L.P. Kubin, Y. Estrin, Evolution of dislocation densities and the critical conditions for the Portevin-Le Châtelier effect, Acta Metall. Mater. 38 (5) (May 1990) 697–708, https://doi.org/10.1016/0956-7151(90)90021-8.
[8] T. Csanádi, N.Q. Chinh, J. Gubicza, T.G. Langdon, Plastic behavior of fcc metals over a wide range of strain: macroscopic and microscopic descriptions and their relationship, Acta Mater. 59 (6) (Apr. 2011) 2385–2391, https://doi.org/10.1016/j.actamat.2010.12.034.
[9] T. Csanádi, N.Q. Chinh, J. Gubicza, G. Vörös, T.G. Langdon, Characterization of stress–strain relationships in Al over a wide range of testing temperatures, Int. J. Plast. 54 (Mar. 2014) 178–192, https://doi.org/10.1016/j.ijplas.2013.08.014.
[10] M. Taheri, H. Weiland, A. Rollett, A method of measuring stored energy macroscopically using statistically stored dislocations in commercial purity aluminum, Metall. Mater. Trans. A 37 (1) (Jan. 2006) 19–25, https://doi.org/10.1007/s11661-006-0148-1.
[11] A.A. Saleh, P. Mannan, C.N. Tomé, E.V. Pereloma, On the evolution and modelling of cube texture during dynamic recrystallisation of Ni–30Fe–Nb–C model alloy, J. Alloys Compd. 748 (Jun. 2018) 620–636, https://doi.org/10.1016/j.jallcom.2018.03.031.
[12] G. Horváth, N.Q. Chinh, J. Gubicza, J. Lendvai, Plastic instabilities and dislocation densities during plastic deformation in Al–Mg alloys, Mater. Sci. Eng. A 445–446 (Feb. 2007) 186–192, https://doi.org/10.1016/j.msea.2006.09.019.
[13] M.F. Ashby, The deformation of plastically non-homogeneous materials, Philos. Mag. J. Theor. Exp. Appl. Phys. 21 (170) (Feb. 1970) 399–424, https://doi.org/10.1080/14786437008238426.
[14] D.A. Hughes, Microstructure evolution, slip patterns and flow stress, Mater. Sci. Eng. A 319–321 (Dec. 2001) 46–54, https://doi.org/10.1016/S0921-5093(01)01028-0.
[15] U.F. Kocks, A statistical theory of flow stress and work-hardening, Philos. Mag. 13 (123) (Mar. 1966) 541–566, https://doi.org/10.1080/14786436608212647.
[16] T.J. Ruggles, T.M. Rampton, A. Khosravani, D.T. Fullwood, The effect of length scale on the determination of geometrically necessary dislocations via EBSD continuum dislocation microscopy, Ultramicroscopy 164 (May 2016) 1–10, https://doi.org/10.1016/j.ultramic.2016.03.003.
[17] B.L. Adams, J. Kacher, EBSD-based microscopy: resolution of dislocation density, computers, Comput. Mater. Contin. 14 (3) (2009) 185–196, https://doi.org/10.3970/cmc.2009.014.185.
[18] C. Zhu, T. Harrington, G.T. Gray, K.S. Vecchio, Dislocation-type evolution in quasi-statically compressed polycrystalline nickel, Acta Mater. 155 (Aug. 2018) 104–116, https://doi.org/10.1016/j.actamat.2018.05.022.
[19] J. Jiang, T.B. Britton, A.J. Wilkinson, Evolution of dislocation density distributions in copper during tensile deformation, Acta Mater. 61 (19) (Nov. 2013) 7227–7239, https://doi.org/10.1016/j.actamat.2013.08.027.

[20] J.F. Nye, Some geometrical relations in dislocated crystals, Acta Metall. 1 (2) (Mar. 1953) 153–162, https://doi.org/10.1016/0001-6160(53)90054-6.
[21] C. Zhu, T. Harrington, V. Livescu, G.T. Gray, K.S. Vecchio, Determination of geometrically necessary dislocations in large shear strain localization in aluminum, Acta Mater. 118 (Oct. 2016) 383–394, https://doi.org/10.1016/j.actamat.2016.07.051.
[22] D.P. Field, C.C. Merriman, N.A. Bonasso, F. Wagner, Quantification of dislocation structure heterogeneity in deformed polycrystals by EBSD, Model. Simul. Mater. Sci. Eng. 20 (2) (Mar. 2012), 024007, https://doi.org/10.1088/0965-0393/20/2/024007.
[23] A. Seret, C. Moussa, M. Bernacki, J. Signorelli, N. Bozzolo, Estimation of geometrically necessary dislocation density from filtered EBSD data by a local linear adaptation of smoothing splines, J. Appl. Crystallogr. 52 (3) (Jun. 2019) 548–563, https://doi.org/10.1107/S1600576719004035.
[24] M. Kamaya, Assessment of local deformation using EBSD: quantification of accuracy of measurement and definition of local gradient, Ultramicroscopy 111 (8) (Jul. 2011) 1189–1199, https://doi.org/10.1016/j.ultramic.2011.02.004.
[25] C. Moussa, M. Bernacki, R. Besnard, N. Bozzolo, Statistical analysis of dislocations and dislocation boundaries from EBSD data, Ultramicroscopy 179 (Aug. 2017) 63–72, https://doi.org/10.1016/j.ultramic.2017.04.005.
[26] W.T. Read, W. Shockley, Dislocation models of crystal grain boundaries, Phys. Rev. 78 (3) (May 1950) 275–289, https://doi.org/10.1103/PhysRev.78.275.
[27] N.A. Fleck, G.M. Muller, M.F. Ashby, J.W. Hutchinson, Strain gradient plasticity: theory and experiment, Acta Metall. Mater. 42 (2) (Feb. 1994) 475–487, https://doi.org/10.1016/0956-7151(94)90502-9.
[28] K.Z. Troost, P. van der Sluis, D.J. Gravesteijn, Microscale elastic-strain determination by backscatter Kikuchi diffraction in the scanning electron microscope, Appl. Phys. Lett. 62 (10) (Mar. 1993) 1110–1112, https://doi.org/10.1063/1.108758.
[29] K. Decroos, J. Sidor, M. Seefeldt, A new analytical approach for the velocity field in rolling processes and its application in through-thickness texture prediction, Metall. Mater. Trans. A 45 (2) (Feb. 2014) 948–961, https://doi.org/10.1007/s11661-013-2021-3.
[30] J.J. Sidor, Assessment of flow-line model in rolling texture simulations, Metals 9 (10) (Oct. 2019) 1098, https://doi.org/10.3390/met9101098.
[31] W.D. Nix, H. Gao, Indentation size effects in crystalline materials: a law for strain gradient plasticity, J. Mech. Phys. Solids 46 (3) (Mar. 1998) 411–425, https://doi.org/10.1016/S0022-5096(97)00086-0.
[32] X. Liu, Y. Sun, T. Nagira, K. Ushioda, H. Fujii, Effect of stacking fault energy on the grain structure evolution of FCC metals during friction stir welding, Acta Metall. Sin. Engl. Lett. 33 (7) (Jul. 2020) 1001–1012, https://doi.org/10.1007/s40195-020-01064-6.
[33] P. Dolzhenko, M. Tikhonova, R. Kaibyshev, A. Belyakov, Peculiarities of DRX in a highly-alloyed austenitic stainless steel, Materials 14 (14) (Jul. 2021) 4004, https://doi.org/10.3390/ma14144004.
[34] V. Randle, Microtexture Determination and its Applications, 2nd ed., Maney for the Institute of Materials, Minerals and Mining, London, 2003.
[35] J.J. Sidor, L.A.I. Kestens, Analytical description of rolling textures in face-centred-cubic metals, Scr. Mater. 68 (5) (Mar. 2013) 273–276, https://doi.org/10.1016/j.scriptamat.2012.10.039.
[36] J.J. Sidor, Effect of hot band on texture evolution and plastic anisotropy in aluminium alloys, Metals 11 (8) (Aug. 2021) 1310, https://doi.org/10.3390/met11081310.
[37] S. El Shawish, J. Hure, Intergranular normal stress distributions in untextured polycrystalline aggregates, Eur. J. Mech. - A/Solids 72 (Nov. 2018) 354–373, https://doi.org/10.1016/j.euromechsol.2018.05.011.
[38] J.G. Sevillano, P.V. Houtte, E. Aernoudt, Large strain work hardening and textures, Prog. Mater. Sci. 25 (2–4) (Jan. 1980) 69–134, https://doi.org/10.1016/0079-6425(80)90001-8.
[39] M.R. Staker, D.L. Holt, The dislocation cell size and dislocation density in copper deformed at temperatures between 25 and 700°C, Acta Metall. 20 (4) (Apr. 1972) 569–579, https://doi.org/10.1016/0001-6160(72)90012-0.
[40] C. Fressengeas, B. Beausir, C. Kerisit, A.L. Helbert, T. Baudin, F. Brisset, M. H. Mathon, R. Besnard, N. Bozzolo, On the evaluation of dislocation densities in pure tantalum from EBSD orientation data, Mater. Technol. 106 (6) (2018) 604, https://doi.org/10.1051/mattech/2018058.
[41] V. Randle, H. Davies, A comparison between three-dimensional and two-dimensional grain boundary plane analysis, Ultramicroscopy 90 (2–3) (Feb. 2002) 153–162, https://doi.org/10.1016/S0304-3991(01)00137-1.
[42] D.P. Field, P.B. Trivedi, S.I. Wright, M. Kumar, Analysis of local orientation gradients in deformed single crystals, Ultramicroscopy 103 (1) (Apr. 2005) 33–39, https://doi.org/10.1016/j.ultramic.2004.11.016.
[43] N.R. Tao, Z.B. Wang, W.P. Tong, M.L. Sui, J. Lu, K. Lu, An investigation of surface nanocrystallization mechanism in Fe induced by surface mechanical attrition treatment, Acta Mater. 50 (18) (Oct. 2002) 4603–4616, https://doi.org/10.1016/S1359-6454(02)00310-5.
[44] D.K. Wilsdorf, Theory of plastic deformation: - properties of low energy dislocation structures, Mater. Sci. Eng. A 113 (Jul. 1989) 1–41, https://doi.org/10.1016/0921-5093(89)90290-6.
[45] W.D. Callister, Fundamentals of Materials Science and Engineering: An Integrated Approach, 2. ed., Wiley, Hoboken, NJ, 2005, p. 252.
[46] A. Roychowdhury, A. Gupta, Material homogeneity and strain compatibility in thin elastic shells, Math. Mech. Solids 22 (7) (Jul. 2017) 1619–1635, https://doi.org/10.1177/1081286515599438.
[47] P.V. Houtte, L. Delannay, I. Samajdar, Quantitative prediction of cold rolling textures in low-carbonsteel by means of the lamel model, Textures Microstruct. 31 (3) (Jan. 1999) 109–149, https://doi.org/10.1155/TSM.31.109.
[48] P.V. Houtte, S. Li, M. Seefeldt, L. Delannay, Deformation texture prediction: from the Taylor model to the advanced Lamel model, Int. J. Plast. 21 (3) (Mar. 2005) 589–624, https://doi.org/10.1016/j.ijplas.2004.04.011.
[49] J.J. Sidor, Deformation texture simulation in Al alloys: continuum mechanics and crystal plasticity aspects, Model. Simul. Mater. Sci. Eng. 26 (8) (Dec. 2018) 085011, https://doi.org/10.1088/1361-651X/aae886.
[50] J. Sidor, A. Miroux, R. Petrov, L. Kestens, Microstructural and crystallographic aspects of conventional and asymmetric rolling processes, Acta Mater. 56 (11) (Jun. 2008) 2495–2507, https://doi.org/10.1016/j.actamat.2008.01.042.
[51] N. Hansen, X. Huang, Microstructure and flow stress of polycrystals and single crystals, Acta Mater. 46 (5) (Mar. 1998) 1827–1836, https://doi.org/10.1016/S1359-6454(97)00365-0.
[52] P. Lehto, Adaptive domain misorientation approach for the EBSD measurement of deformation induced dislocation sub-structures, Ultramicroscopy 222 (Mar. 2021) 113203, https://doi.org/10.1016/j.ultramic.2021.113203.
[53] B. Jung, H. Lee, H. Park, Effect of grain size on the indentation hardness for polycrystalline materials by the modified strain gradient theory, Int. J. Solids Struct. 50 (18) (Aug. 2013) 2719–2724, https://doi.org/10.1016/j.ijsolstr.2013.05.002.
[54] Y. Huang, F.J. Humphreys, Measurements of grain boundary mobility during recrystallization of a single-phase aluminium alloy, Acta Mater. 47 (7) (May 1999) 2259–2268, https://doi.org/10.1016/S1359-6454(99)00062-2.